

See discussions, stats, and author profiles for this publication at: <https://www.researchgate.net/publication/216439233>

# Enhanced Photoelectrochemical Response of BaTiO<sub>3</sub> with Fe Doping: Experiments and First-Principles Analysis

ARTICLE in THE JOURNAL OF PHYSICAL CHEMISTRY C · DECEMBER 2011

Impact Factor: 4.77 · DOI: 10.1021/jp202863a

CITATIONS

15

READS

131

## 11 AUTHORS, INCLUDING:



**Surbhi Choudhary**

DPG ITM Engg College, Gurgaon

18 PUBLICATIONS 83 CITATIONS

SEE PROFILE



**Vibha R. Satsangi**

Dayalbagh Educational Institute

86 PUBLICATIONS 856 CITATIONS

SEE PROFILE



**Rohit Shrivastav**

Dayalbagh Educational Institute

103 PUBLICATIONS 1,173 CITATIONS

SEE PROFILE



**Sahab Dass**

Dayalbagh Educational Institute

107 PUBLICATIONS 1,235 CITATIONS

SEE PROFILE

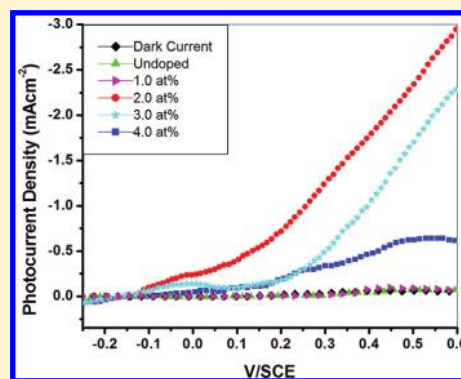
# Enhanced Photoelectrochemical Response of BaTiO<sub>3</sub> with Fe Doping: Experiments and First-Principles Analysis

Sumant Upadhyay,<sup>†</sup> Jaya Shrivastava,<sup>†</sup> Anjana Solanki,<sup>†</sup> Surbhi Choudhary,<sup>†</sup> Vidhika Sharma,<sup>†</sup> Pushpendra Kumar,<sup>†</sup> Nirupama Singh,<sup>†</sup> Vibha R. Satsangi,<sup>‡</sup> Rohit Shrivastav,<sup>†</sup> Umesh V. Waghmare,<sup>§</sup> and Sahab Dass<sup>\*,†</sup>

<sup>†</sup>Department of Chemistry and <sup>‡</sup>Department of Physics & Computer Sciences, Dayalbagh Educational Institute, Agra-282 110, India

<sup>§</sup>Theoretical Sciences Unit, Jawaharlal Nehru Centre for Advanced Scientific Research, Jakkur, Bangalore-560 064, India

**ABSTRACT:** We use a combination of experiments and first-principles density functional theory based calculations in a study of the photoelectrochemical properties of Fe-doped BaTiO<sub>3</sub> nanopowder. BaTiO<sub>3</sub> with 0.5–4.0 atom % Fe doping is synthesized via a polymeric precursor route and characterized with X-ray diffractometry (XRD), scanning electron microscopy (SEM), high-resolution transmission electron microscopy (HR-TEM), UV–vis spectroscopy, and Mössbauer spectroscopy. We find a red shift of 0.39 eV in the UV–vis spectrum and hence an improved photoelectrochemical activity in the visible range upon Fe doping in BaTiO<sub>3</sub>. The origin of the observed activity in the visible range is traced through the calculated electronic structure to the electronic states associated with Fe at energies within the band gap. A reasonable agreement between the changes in measured spectra and those in calculated electronic structure augurs well for a judicious use of first-principles calculations in screening of dopants in the design of doped oxide materials with enhanced photoelectrochemical activity, such as that of Fe-doped BaTiO<sub>3</sub> demonstrated here.



## 1. INTRODUCTION

Hydrogen is a recyclable and clean fuel as it generates water after its use in combustion, and the water can be split to generate hydrogen back. The latter is a crucial step and can be facilitated through use of a photocatalyst in splitting of water into hydrogen gas by accessing solar energy, another important source of energy for the planet. Indeed, it is important to discover and develop a photocatalytic material for this process. An optimal material should have a band gap that allows absorption of light in the visible range and remain stable when in contact with water. In addition, it should be nontoxic, abundant, and easily processable into a desired shape. In 1972, Fujishima and Honda first reported the photoassisted splitting of water into H<sub>2</sub> and O<sub>2</sub> on TiO<sub>2</sub>, providing the possibility to convert solar energy into chemical energy in a renewable and cheap way.<sup>1–6</sup> Since then, considerable efforts have been devoted to related areas of research, such as photocatalysis, dye-sensitized solar cells, etc.<sup>7–16</sup> Hydrogen, generated by splitting water using solar energy, is even called “solar hydrogen”. It is a kind of clean and low-cost fuel.<sup>17</sup> Thus, development of stable and efficient photosensitive materials becomes key to the future of “solar hydrogen”. In the search for a suitable photoelectrode and photocatalyst, perovskite-based metal oxides (ABO<sub>3</sub>) have been the subject of extensive studies during the past two decades, because they offer a wide range of possibilities for tailoring their structure through cationic substitutions at either A or B sites and tuning their optical and electrical properties.<sup>18</sup>

BaTiO<sub>3</sub> exhibits a mixed ionic–covalent chemical bonding between Ba and O and a strong hybridization between the

d states of Ti and the p states of O, leading to sensitivity of its structure to external conditions such as pressure, and it is one of the most commonly used titanates in splitting of water.<sup>19</sup> The advantages of BaTiO<sub>3</sub> as a photoelectrode in hydrogen production by photoelectrochemical water splitting include its (i) high resistance to corrosion and photocorrosion in aqueous media, (ii) easy availability at low cost, (iii) environmental friendliness, (iv) well-matched energy band edges with the redox level of water, and (v) electronic properties that can be varied by changing the lattice defect chemistry or the oxygen stoichiometry.<sup>20</sup> However, BaTiO<sub>3</sub>, with an energy band gap of about 3.2 eV, mostly absorbs in the ultraviolet portion of the solar spectrum and only a small amount of visible light.<sup>21</sup> For efficient photoelectrochemical activity it is necessary to modify BaTiO<sub>3</sub> and extend its photoresponse to the visible part of the spectrum.<sup>22</sup> While many methods have been proposed to address this issue, doping with ions is one of the most promising strategies for sensitizing BaTiO<sub>3</sub> to visible light.<sup>23</sup> A few reports suggest the possibility of using Fe-doped BaTiO<sub>3</sub> for photoelectrochemical generation of hydrogen.<sup>24,25</sup> As a thorough experimental analysis of BaTiO<sub>3</sub> with each type of dopant is quite demanding, it can be quite effective to use first-principles-based density functional theory calculations in short-listing dopants that have promise for enhanced photocatalytic activity of BaTiO<sub>3</sub>. Such calculations

**Received:** March 28, 2011

**Revised:** October 27, 2011

**Published:** October 27, 2011

are quite useful in semiquantitative determination of the trends in band gaps upon doping a given material.<sup>26–28</sup>

In the present study, substitution of  $\text{Fe}^{3+}$  at B site as confirmed by Mössbauer spectroscopy was attempted to modify the electronic and photoelectrochemical properties of  $\text{BaTiO}_3$  and a comparative study was carried out on  $\text{BaTiO}_3$  and Fe-doped  $\text{BaTiO}_3$  nanoparticles in order to clarify the role of  $\text{Fe}^{3+}$  metal ions played in enhancement of the photocatalytic activity of  $\text{BaTiO}_3$ . Attention was focused not only on the experimentally obtained X-ray diffraction (XRD), scanning electron microscopy (SEM), high-resolution transmission electron microscopy (HRTEM), ultraviolet–visible (UV–vis) absorption spectra, Mössbauer spectroscopy, and photoelectrochemical performance results but also on first-principles calculations based on density functional theory (DFT). We determined the electronic structure of undoped and Fe-doped  $\text{BaTiO}_3$  and attempted to develop an understanding of the mechanism of the enhanced photoelectrochemical activity for Fe-doped  $\text{BaTiO}_3$ . Our work, giving a qualitative idea of the errors in theoretical predictions through comparison with experiments, will also serve as the basis for use of such calculations in the design of doped oxides as photocatalysts.

## 2. EXPERIMENTAL METHODS

**2.1. Materials Preparation.** Fe-doped  $\text{BaTiO}_3$  nanopowder was synthesized by the polymeric precursor route.<sup>29,30</sup> The titanium solution was prepared by dissolving titanium tetraisopropoxide (Aldrich, 97%) in a solution of citric acid (Aldrich, 99.9%) and ethylene glycol (Aldrich, 99.9%) mixed in a molar ratio of 1:4. The appropriate amount of required stoichiometry of  $\text{BaCO}_3$  (Aldrich, 99%) and 0.5–2.0 atom % of  $\text{Fe}_2\text{O}_3$  (Aldrich, 97%) were dissolved in the above titanium solution. This solution was heated at 90 °C with constant stirring until it became a clear transparent yellow solution. This solution was heated at 200 °C for 5 h in an oven to promote polymerization and remove solvents with continued heating at 200 °C; the solution become more viscous accompanied by a color change from pale yellow to brown. There was no precipitation or turbidity observed, and finally, the viscous mass solidified into a dark brown, glassy resin. Charring the resin at 400 °C for 2 h in an electric furnace resulted in a black solid mass that was lightly ground into a powder using an agate mortar and a pestle. The precursor obtained was sintered at 500, 700, and 900 °C in air for 5 h in an  $\text{Al}_2\text{O}_3$  boat with intermittent grindings. Phase synthesis was monitored after every sintering using XRD.

**2.2. Materials Characterization.** Powder X-ray diffraction (XRD) patterns were obtained on a D8 Advance X-ray diffractometer (Bruker, Germany) using  $\text{Cu K}\alpha$  radiation at a scan rate of  $0.02^\circ 2\theta \text{ s}^{-1}$ . Scanning electron microscopy (SEM) and energy-dispersive X-ray spectroscopy were performed by an MV 2300T/40 field emission SEM model Tescan Vega using an accelerating voltage of 25 kV at a working distance of ~10 mm. High-resolution transmission electron microscopy (HRTEM) analysis was conducted with the use of JEOL 1230, Japan. UV–vis spectra were obtained using a spectrophotometer JASCO model V-530, Japan.

The Fe valence state, occupational site, and site ratio in the perovskite lattice were recorded using a Mössbauer spectrometer for a representative sample [Mössbauer spectrometer System (MC1002), Nucleonix Systems Pvt. Ltd., Hyderabad, India] operated in constant acceleration mode (triangular wave) in

transmission geometry. The source employed is Co-57 in a Rh matrix of strength 50 mCi. Calibration of the velocity scale is done by using  $\alpha\text{-Fe}$  metal foil. The outer line width of the calibration spectra is 0.29 mm/s. Mössbauer spectra were fitted by a least-squares fit (MOSFIT) program assuming Lorentzian line shapes. The result of the isomer shift is relative to  $\alpha\text{-Fe}$  metal foil.

**2.3. Photoelectrochemical Performance.** Powered samples of Fe-doped and undoped  $\text{BaTiO}_3$  were compacted into pellets using a pelletization unit (Technosearch Instruments, Mumbai, India) at 5 tonn pressure followed by sintering at 500 °C for 2 h. The electrical contacts on all pellet samples for PEC measurements were made through a fine copper wire loop attached to the back side of the pellet sample with conducting silver paint. The back sides of each pellet including the copper wire loop were covered and sealed by an epoxy resin (Hysol, Singapore) which was nonconducting and opaque. The entire structure was heated in an oven at 70–80 °C to ensure complete drying.

A three-electrode potentiostat system was used to measure the photoelectron current, which allowed measurement of the electron and hole pair formation as a function of the externally applied potential necessary for water splitting. The photoelectrodes were placed in the electrolyte (0.1 M, NaOH), while potentiostatic control was maintained with a PAR Versastat II at a scan rate of 25 mV/s. A large area platinum wire mesh was used as the counter electrode and Ag/AgCl as the reference electrode. The illumination source employed was a 150W-Oriel 6690 Xe arc UV–vis lamp directed at the quartz photoelectrochemical cell with an intensity of  $0.18 \text{ W/cm}^2$ . A water filter was used to remove the IR energy and avoid overheating. The photocurrent densities were calculated using the difference between the light off (dark current) and the light-on currents acquired consecutively. Resistivity and open circuit photovoltage ( $V_{oc}$ ) was calculated for all samples from the current–voltage characteristics recorded under dark conditions. To obtain the Mott–Schottky curves, the capacitance ( $C$ ) at the semiconductor/electrolyte junction with an ac signal frequency of 1 kHz was measured using a LCR meter (Agilent Technology, model 4263 B, Singapore) at varying electrode potentials in the same three-electrode configuration. These curves are used to calculate the flatband potentials and donor density for all samples.

**2.4. Computational Details.** All calculations were performed using the Quantum Espresso implementation of density functional theory (DFT)<sup>31</sup> within the generalized gradient approximation (GGA). The interaction between the valence electrons and the nucleus core electrons was modeled with ultrasoft pseudopotentials.<sup>32</sup> We simulated the effects of Fe doping using a  $2 \times 2 \times 2$  (40-atom)  $\text{BaTiO}_3$  supercell and replacing one Ti atom by an Fe atom, amounting to 12.5% doping amount. Calculated crystal parameters of the unit bulk tetragonal  $\text{BaTiO}_3$  are  $a = 3.9904 \text{ \AA}$  and  $c = 4.0689 \text{ \AA}$ , in good agreement with experimental data.<sup>33</sup> A Monkhorst-pack<sup>34</sup> mesh of  $4 \times 4 \times 4$   $k$  points was used in sampling the integrals over the Brillouin zone, and a much finer mesh was used in accurate determination of the density of the electronic states. Kohn–Sham wave functions were represented in a plane-wave basis with an energy cutoff energy of 30 Ry, and the charge density was represented with a plane-wave basis with a cutoff of 180 Ry. Structural optimization was carried out using Hellman–Feynman forces to minimize the total energy. To check the convergence of our results, we carried out test calculations with higher energy cutoffs on the plane-wave basis and finer meshes of  $k$  points, making sure that there are

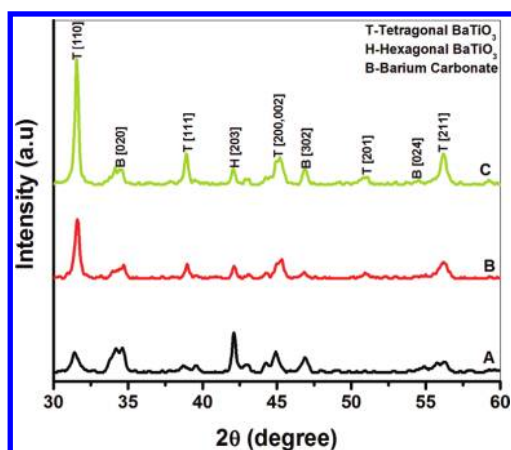


**Figure 1.** X-ray diffraction patterns of the powder samples of undoped  $\text{BaTiO}_3$  (A = 500 °C, B = 700 °C, C = 900 °C) prepared at different sintering temperatures.

negligible changes in energy (the difference between the total energies is less than 0.02%), and the structure and electronic structure are essentially unchanged. Electronic structures reported here have been calculated at the optimized structures.

### 3. RESULTS AND DISCUSSION

**3.1. XRD Studies.** The phase structure and purity of the as-fabricated samples were studied by powder X-ray diffraction (XRD). Figures 1 and 2 show the XRD patterns of  $\text{BaTi}_{1-x}\text{Fe}_x\text{O}_3$  ( $0.0 \leq x \leq 0.02$ ) as a function of sintering temperature and doping concentration. All diffraction peaks can be well indexed to  $\text{BaTiO}_3$  (JCPDS card no. 031-0174), suggesting successful preparation of  $\text{BaTiO}_3$  crystals. It is revealed that as the sintering temperature increased to 900 °C the intensity of the unreacted phases like barium carbonate was reduced, and the counts due to tetragonal  $\text{BaTiO}_3$  phase increased due to an increase in the crystallinity of the sample. Formation of impurity phases such as hexagonal  $\text{BaTiO}_3$  along with marginal cubic phase were observed in the sample sintered at 500 °C as shown in curve c of Figure 1. The tetragonal phase of  $\text{BaTiO}_3$  is predominantly present when the sample was sintered above 600 °C. Complete transformation of precursor into tetragonal  $\text{BaTiO}_3$  along with small peaks of hexagonal and cubic phase at 900 °C for 5 h was confirmed by the XRD pattern of the sample, which matches with that of tetragonal  $\text{BaTiO}_3$  also marked by the presence of distinct 002 and 200 peaks in curve c in Figure 1. Maximum crystallinity was obtained in 2.0 atom % Fe-doped samples sintered at 900 °C; similar results have been obtained by other researchers also.<sup>35</sup> The XRD pattern of  $\text{BaTi}_{1-x}\text{Fe}_x\text{O}_3$  as a function of doping concentration is shown in Figure 2, where all Fe-substituted samples are single phase and crystallized in the perovskite  $\text{BaTiO}_3$  tetragonal lattice.

As calculated by the Debye–Scherrer equation, crystallite diameters for the tetragonal phase of the 110 peak as a function of Fe substitution and sintering temperatures are listed in Table 1. The crystallite diameter of doped  $\text{BaTiO}_3$  gradually decreases with increasing concentration of Fe. Thus, it appears that  $\text{Fe}^{3+}$  with a given concentration is soluble in  $\text{BaTiO}_3$  lattice and the dopant influences the growth of a secondary phase in a peculiar way. As seen from Table 1, the sample with Fe substitution has a crystallite size lower than undoped  $\text{BaTiO}_3$ . We suppose that  $\text{Fe}^{3+}$

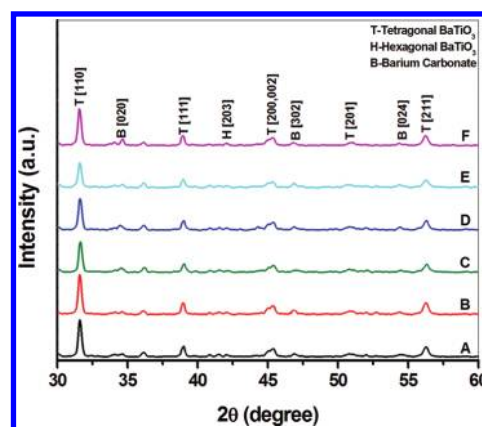


**Figure 2.** X-ray diffraction pattern of Fe-doped  $\text{BaTiO}_3$  (A = undoped, B = 0.5 atom %, C = 1.0 atom %, D = 2.0 atom %, E = 3.0 atom %, F = 4.0 atom % sintered at 900 °C).

**Table 1.** Crystallite Size of  $\text{BaFe}_x\text{Ti}_{(1-x)}\text{O}_3$  Samples As Calculated from XRD Line Width Using the Scherrer Equation as a Function of Fe Content ( $x$ ) and Sintering Temperatures

samples	$\text{BaTiO}_3$ sintered at 500 °C	$\text{BaTiO}_3$ sintered at 700 °C	$\text{BaTiO}_3$ sintered at 900 °C
undoped $\text{BaTiO}_3$	20 nm	32 nm	43 nm
0.5 atom % Fe	26 nm	30 nm	42 nm
1.0 atom % Fe	24 nm	27 nm	41 nm
2.0 atom % Fe	18 nm	23 nm	36 nm
3.0 atom % Fe	16 nm	20 nm	34 nm
4.0 atom % Fe	14 nm	24 nm	32 nm

ions inhibit further grain growth, leading to the decreasing crystallite diameter. This is attributed to the aliovalent substitution of Ti by Fe at B sites, such that microstructural defects and nonstoichiometry are generated as a result of substitution.<sup>36</sup> Crystallite size as a function of sintering temperature was also calculated by the Debye–Scherrer equation using the XRD line width for all Fe-doped and undoped  $\text{BaTiO}_3$ . The growth in crystallite size with an increase in sintering temperature as evident from Table 1 is attributed to the sintering effects. Taguchi et al.<sup>37</sup> demonstrated that the crystallite size decreases in the perovskite-type  $(\text{La}_{1-x}\text{Ca}_x)\text{FeO}_3$  samples, and such samples with smaller crystallite size exhibited a higher catalytic activity. These results suggest that the substitution-induced microstructural defects and nonstoichiometry created on lattice reorganization during synthesis also play a role in deciding the morphology of the sample.

**3.2. Morphology and Growth Mechanism.** The stoichiometry of the prepared powder is confirmed by EDX (Figure 3a). The observed average atom % values from the data collected at three different locations are in agreement with the expected values for  $\text{BaTiO}_3$  within experimental error.

SEM (Figure 3b and 3c) analysis reveals that both Fe-doped and undoped  $\text{BaTiO}_3$  particles are approximately spherical in shape. SEM analysis reveals formation of particles with different shapes and sizes for the undoped  $\text{BaTiO}_3$  (Figure 3b). It seems appropriate to consider that the particles which appear in SEM images are, in fact, aggregates of grains agglomerated in undoped samples, whereas Fe incorporation has inhibited grain growth



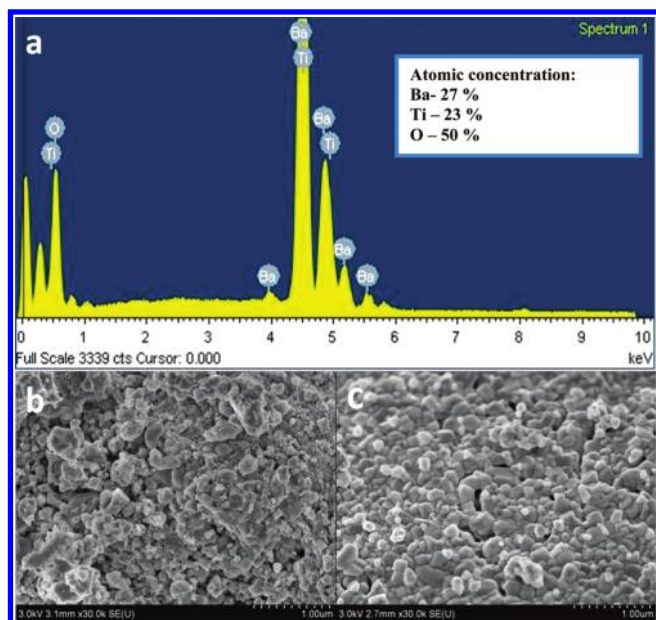


**Figure 3.** SEM micrographs: a = EDX of undoped BaTiO<sub>3</sub>, b = SEM of undoped BaTiO<sub>3</sub>, and c = SEM of 2.0 atom % Fe-doped BaTiO<sub>3</sub>.

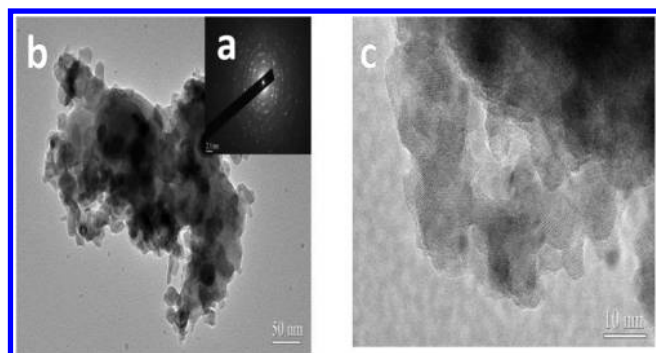


**Figure 4.** HR-TEM images of 2.0 atom % Fe-doped BaTiO<sub>3</sub> sintered at 900 °C.

and prevented agglomeration of sample prepared under identical conditions (Figure 3c). Our results are in agreement with the work reported by Gupta et al.,<sup>38</sup> where Fe doping resulted in smaller unagglomerated grains of ZnO samples with well-defined spherical shaped particles arranged in a regular fashion. The random distribution of grains, in projection and size, only suggests a random nucleation mechanism, and random orientation of grains shows that grain growth is isotropic in doped samples, showing complete solubility of dopant ion in BaTiO<sub>3</sub> lattice.

HR-TEM (Figure 4) analysis also exhibits better crystallinity, a well-defined shape, and the homogeneous nature of the powders. Figure 4a shows the electron diffraction pattern of 2.0 atom % substituted sample where it was indexed and found to be in tetragonal BaTiO<sub>3</sub>. Homogeneous formation of 10–26 nm nano-sized crystallites by polymeric precursor synthesis observed from HR-TEM (Figure 4b) is in agreement with the XRD results. HR-TEM in Figure 4c shows that atoms are arranged periodically in well-defined planes inside nanosized particles of Fe-doped BaTiO<sub>3</sub>.

**3.3. Band Gap Measurements.** The diffuse and total reflectance (Figure 5) of the samples was measured as a function of

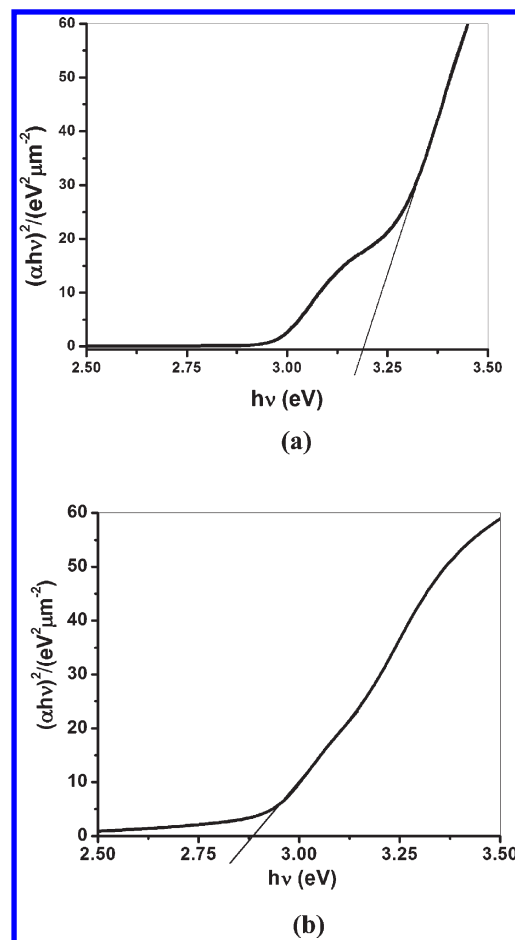


**Figure 5.** UV–vis spectra of (a) undoped and (b) 2.0 atom % Fe-doped BaTiO<sub>3</sub> sintered at 900 °C.

wavelength from 200 to 800 nm using the diffuse reflectance attachment of a Perkin-Elmer spectrophotometer. The optical band gap of samples was calculated from  $\text{tauc}$  plots (Figure 5), and the best fit was found for the indirect band gap transition rather than the direct band gap with values of 3.11 eV for the undoped and 2.81 eV for 2.0 atom % Fe-doped BaTiO<sub>3</sub>. This observation is in agreement with that of F. M. Pontes et al.<sup>39</sup> With the increase in doped amount of Fe<sup>3+</sup> in BaTiO<sub>3</sub> the UV–vis spectra show a red shift and band gap lowering up to 2.81 eV. The variation of the band gap energy with the doping concentration is given in Table 2. The charge transfer transition between Fe 3d electrons and the conduction band (CB) may explain the appearance of the red shift. The absorption patterns of BaTi<sub>1-x</sub>Fe<sub>x</sub>O<sub>3</sub> ( $0.0 \leq x \leq 0.02$ ) are highly dependent on the dopant concentration as shown in Figure 5. The result has been further confirmed by first-principles theoretical calculations. This red shift in doped BaTiO<sub>3</sub> increases the number of photogenerated electrons and holes to participate in the photocatalytic reaction, which support the enhanced photocatalytic activity of Fe-doped BaTiO<sub>3</sub>.

**3.4. Mössbauer Spectroscopy.** The room-temperature Mössbauer spectrum for 2.0 atom % Fe-doped BaTiO<sub>3</sub> sintered at 900 °C is shown in Figure 6. The observed spectrum can be fitted with one magnetic sextet and a paramagnetic doublet. The values of the Mössbauer parameters for the sextet such as the hyperfine field ( $H_{\text{hf}}$ ), quadrupole splitting ( $\Delta E_Q$ ), isomer

**Table 2.** Measured Parameters of Optical and Photoelectrochemical Properties for Undoped and Fe-Doped BaTiO<sub>3</sub> Samples Sintered at 900 °C

samples	band gap energy (eV)	open-circuit photovoltage $V_{oc}$ (V/SCE)	photocurrent density at 0.5 V/SCE (mA/cm <sup>2</sup> )
undoped BaTiO <sub>3</sub>	3.11	0.10	0.07
0.5 atom % Fe	3.06	0.16	0.12
1.0 atom % Fe	2.94	0.23	0.14
2.0 atom % Fe	2.81	0.36	2.55
3.0 atom % Fe	2.84	0.26	1.70
4.0 atom % Fe	2.89	0.19	0.62

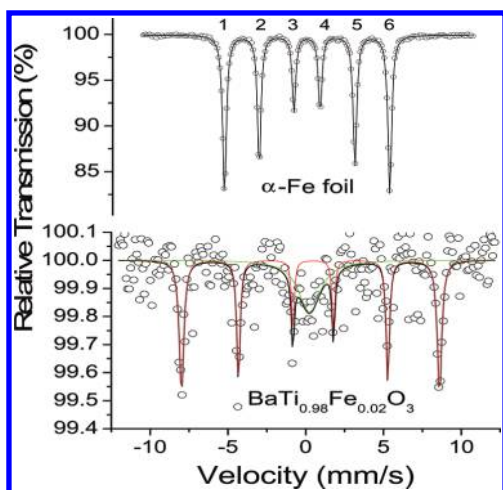


**Figure 6.** Room-temperature Mössbauer spectrum of 2.0 atom % Fe-doped BaTiO<sub>3</sub> sintered at 900 °C. Component spectra are represented by dotted lines.

shift ( $\delta$ ), outer line width ( $\Gamma$ ), and area (%) derived from the Mössbauer spectrum are 515.3 kG ( $H_{hf}$ ), 0.0851 mm/s ( $\Delta E_Q$ ), 0.476 mm/s ( $\delta$ ), 0.346 mm/s ( $\Gamma$ ), and 67.2%, respectively. Mössbauer parameters for the doublet such as the quadrupole splitting ( $\Delta E_Q$ ), isomer shift ( $\delta$ ), outer line width ( $\Gamma$ ), and area (%) derived from the Mössbauer spectrum are 0.004 mm/s ( $\Delta E_Q$ ), 0.241 mm/s ( $\delta$ ), 1.728 mm/s ( $\Gamma$ ), and 32.8%, respectively.

Isomer shift ( $\delta$ ) values for the sextet and paramagnetic doublet are 0.476 and 0.241 mm/s, respectively, with respect to  $\alpha$ -Fe ( $\delta = 0.00$  mm/s). It indicates that Fe is in Fe<sup>3+</sup> ionic state.<sup>40–43</sup> The isomer shift is related to the s-electron density. A higher isomer shift means that the s-electron density at the Fe nucleus will be lower. The isomer shift of the tetrahedral site is lower than that of octahedral site. It suggests that the Fe<sup>3+</sup> ion in the tetrahedral site has more s-electron density than that in the octahedral site. It results in a shorter Fe–O distance in the tetrahedral site than that in the octahedral site. The chemical isomer shift increases in the sequence  $\delta$  (tetrahedral Fe<sup>3+</sup>) <  $\delta$  (octahedral Fe<sup>3+</sup>) <  $\delta$  (tetrahedral Fe<sup>2+</sup>) <  $\delta$  (octahedral Fe<sup>2+</sup>). These results suggest that the sextet belongs to the octahedral site.

The presence of Fe<sup>2+</sup> was ruled out based on the absence of absorption at a higher velocity (a center shift of at least 1.0 mm/s relative to  $\alpha$ -Fe would be expected, e.g., ref 44). The presence of Fe metal is also ruled out based on the absence of an absorption

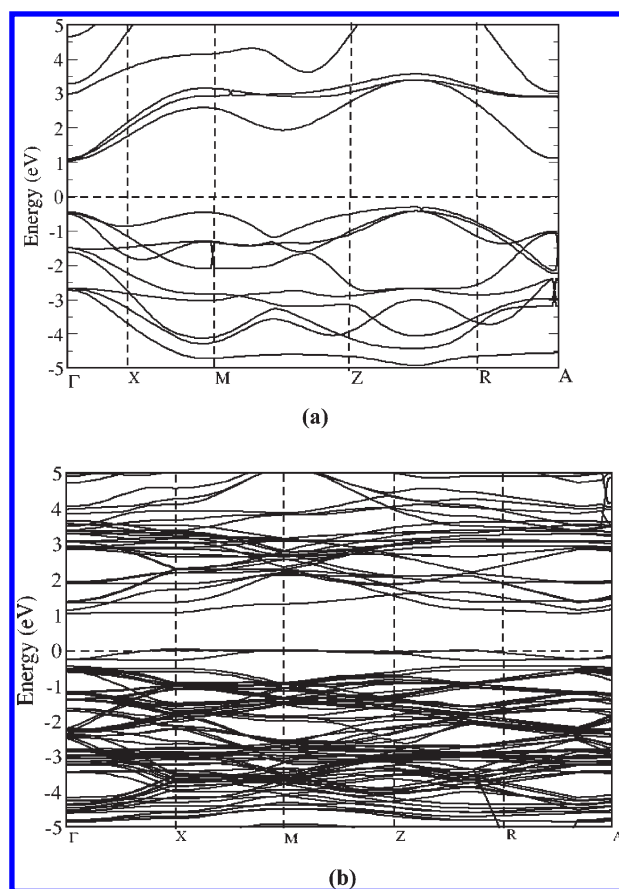


**Figure 7.** Electronic band structure for (a) undoped BaTiO<sub>3</sub> and (b) Fe-doped BaTiO<sub>3</sub>. Fermi energy is set at zero.

**Table 3.** Change in Band Gap for Undoped and Fe-Doped BaTiO<sub>3</sub> at Different High-Symmetry Points in Brillouin Zone

undoped BaTiO <sub>3</sub>		Fe-doped BaTiO <sub>3</sub>	
high-symmetry points in Brillouin zone	band gap	high-symmetry points in Brillouin zone	band gap
$\Gamma$ –M	1.80 eV	$\Gamma$ –X	1.23 eV
$\Gamma$ – $\Gamma$	1.85 eV	$\Gamma$ – $\Gamma$	1.54 eV

line between  $-7.96$  and  $-4.33$  mm/s velocity and no other sextet observed in the Mössbauer spectrum. In the Fe metal foil spectrum (single sextet) the first line absorption position is at  $-5.312$  mm/s velocity. The quadrupole splitting ( $\Delta$ ) value for the doublet is almost 0.00 mm/s with respect to  $\alpha$ -Fe, suggesting that Fe<sup>3+</sup> ions show cubic symmetry of a polyhedron. The quadrupole splitting for both Fe<sup>2+</sup> and Fe<sup>3+</sup> in sites of accurately cubic symmetry is zero and for noncubic sites  $\Delta(\text{Fe}^{3+}) \ll \Delta(\text{Fe}^{2+})$ . The value of the isomer shift and quadrupole splitting of the doublet suggest that Fe is in the Fe<sup>3+</sup> ionic state.

There is superposition of the sextet and doublet patterns in the Mössbauer spectrum. The doublet pattern arises from the presence of a superparamagnetic fraction, whereas the sextet pattern comes from the presence of a ferromagnetic fraction. However, the relative percentage of sextet to doublet patterns was found to be 67:33, indicating that the superparamagnetic fraction is small.

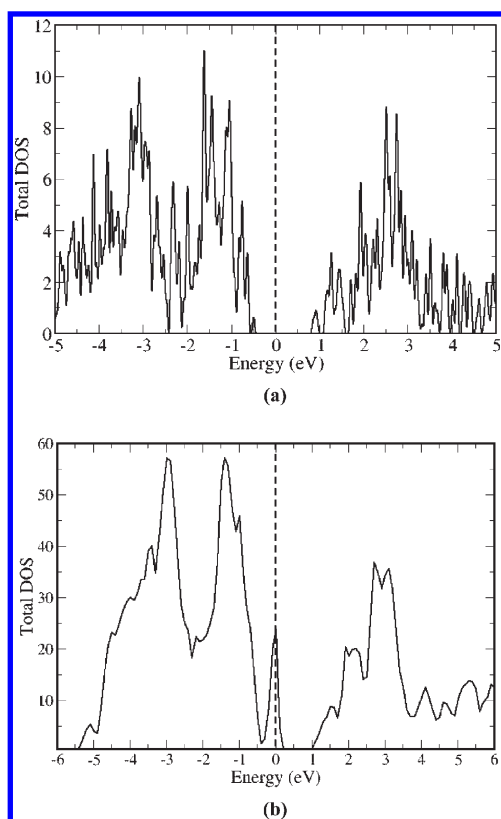


**Figure 8.** Total density of states plots of (a) undoped and (b) Fe-doped BaTiO<sub>3</sub>. Fermi energy is set at zero.

**3.5. Band Structure and Photoabsorption Properties.** The electronic structure of the oxide semiconductor plays a crucial role in determining its photocatalytic activity. In the present study, the electronic structures of BaTiO<sub>3</sub> and BaTiO<sub>3</sub> doped with 12.5% iron were determined with DFT calculations. Band structures of undoped and doped systems for the 40-atom supercell are shown in Figure 7a and 7b for undoped BaTiO<sub>3</sub> and Fe-doped BaTiO<sub>3</sub>. Calculated band gaps are listed in Table 3.

Typically, band gaps estimated with DFT are smaller than the experimental values,<sup>45</sup> not surprisingly because DFT solves the electronic ground state problem. Accurate estimation of absolute values of band gaps requires one to go beyond density functional theory by including self-interaction corrections or using hybrid functional. While conduction band properties are not accurately captured, those associated with valence bands and the corresponding offsets are described reasonably well within DFT. In the present work, we were more interested in how band gaps change with doping rather than their absolute values and find the changes in band gap with Fe doping are

$$\Delta E_g = 0.31 \text{ eV (theoretical)}$$

$$\Delta E_g = 3.2 - 2.81 = 0.39 \text{ eV (experimental)}$$

Our results for the band structures obtained with DFT calculations show that the top of the valence band and the bottom of the conduction band of undoped BaTiO<sub>3</sub> are at the M point and  $\Gamma$  point of the Brillouin zone, respectively (Figure 7a and 7b), suggesting that pure BaTiO<sub>3</sub> is an indirect band gap material. However, the band gap is significantly reduced in the Fe-doped BTO because of the appearance of the defect band at the Fermi

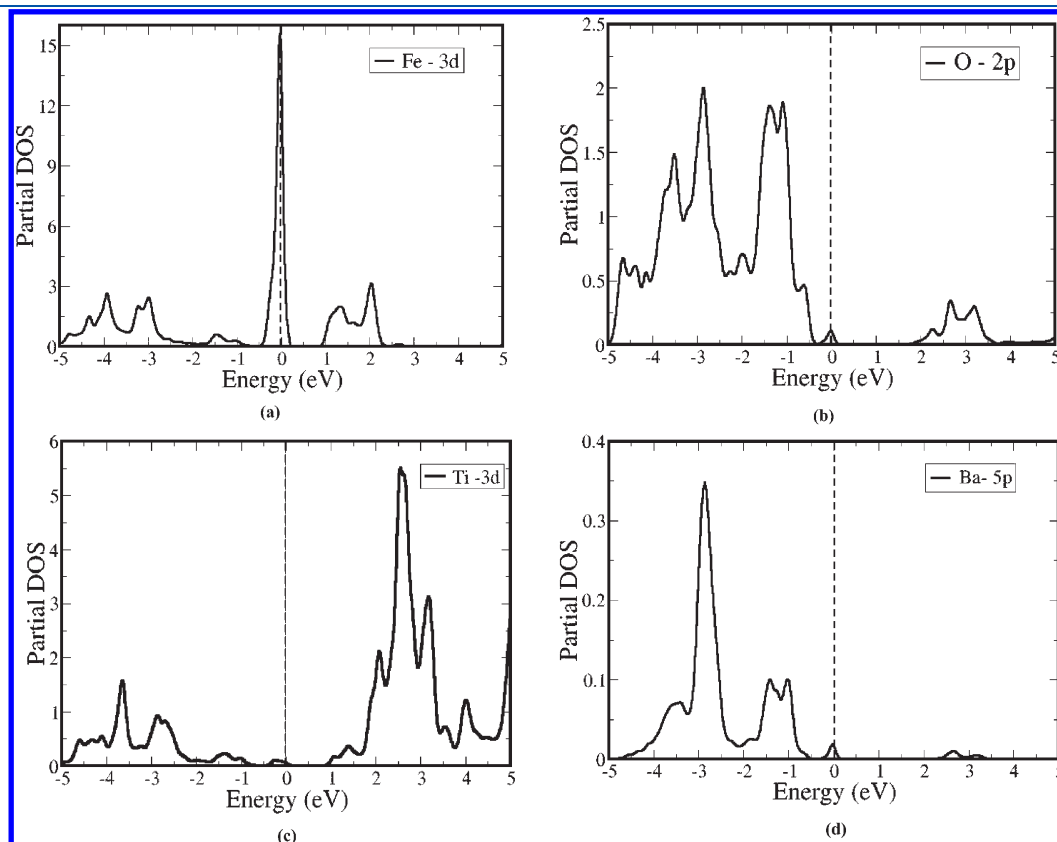


**Figure 9.** Partial density of states (PDOS) of (a) Fe, (b) O, (c) Ti, and (d) Ba ions. Fermi energy is set at zero.

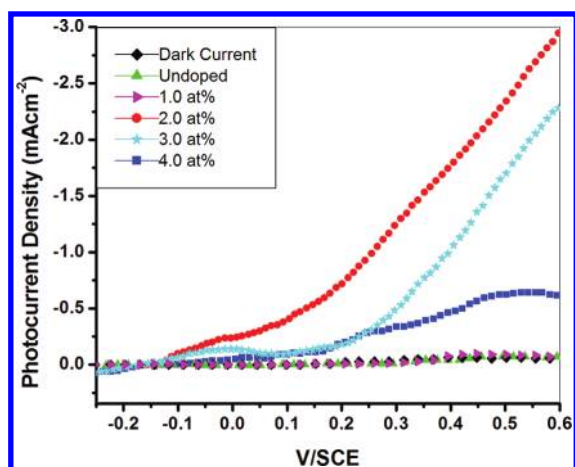


**Figure 10.** Photoelectrochemical characteristics of undoped and 0.5, 1.0, and 2.0 atom % Fe-doped BaTiO<sub>3</sub> sintered at 900 °C.

energy which is closer to the valence band. The band gap changes to the  $\Gamma$ -X point of the Brillouin zone, keeping it still an indirect gap material. Consequently, the gap is reduced to 1.23 eV. The total density of states (DOS) in Figure 8a and 8b demonstrates that a sharp peak appears near the Fermi energy, corresponding to the defect band associated with the 3d states of Fe. It is clear from the partial DOSs in Figure 9a–d that this sharp peak in the total DOS essentially comes from Fe impurity. These first-principles calculations are consistent with the large red shift in the UV–vis spectra.

**3.6. Photocurrent Investigation.** On studying the PEC response of various samples prepared at different sintering temperatures and varying doping concentrations of Fe it was found that sample doped with 2.0 atom % Fe sintered at 900 °C exhibited the highest photocurrent density. The photocurrent density obtained with undoped BaTiO<sub>3</sub> sample sintered at 900 °C was 0.07 mA cm<sup>-2</sup> at 0.5 V/SCE, whereas the maximum photocurrent density recorded in the sample doped with 2.0 atom % Fe was 2.55 mA cm<sup>-2</sup> at 0.5 V/SCE (Figure 10) (Table 2). Compared to other researchers,<sup>46–48</sup> we recorded a good photocurrent density in the present experimentation. Doping of iron into the BaTiO<sub>3</sub> structure caused a decrease in resistivity, resulting in a decrease in the numbers of recombination centers. It is supposed that the decrease in the number of recombination centers results in an increase in the photocarriers lifetime, leading to the increase in photoconductivity.<sup>49</sup> Moreover, the red shift caused due to Fe doping resulted in more absorption in the visible region, causing an increase in photocurrent. Thus, it was observed that 2.0 atom % is the optimal doping level above and below which (i.e., 0.5, 1.0, 3.0, and 4.0 atom % Fe doping) the photocurrent density decreased. The maximum value of the open-circuit photovoltage obtained for this sample also supports the significant rise in the photocurrent density as compared to the undoped BaTiO<sub>3</sub> sample (Table 2). The sharp decrease in the resistivity values for 2.0 atom % Fe-doped sample (Table 4) also accounts for the better performance of the sample upon Fe doping. On the other hand, a higher concentration of doping would provide more defect-scattering/recombination properties inhibiting the increased separation efficiency.<sup>50</sup>

The good photoresponse of this sample has also been supported by the maximum value of the flatband potential and donor

**Table 4.** Electrical and Photoelectrochemical Properties of All Undoped and Fe-Doped BaTiO<sub>3</sub> Samples Deduced from Mott–Schottky and Current–Voltage Curves

samples	donor density, $N_d$ (cm <sup>-3</sup> )	flatband potential, $V_{fb}$ (V/SCE)	resistivity ( $\Omega$ cm)
undoped BaTiO <sub>3</sub>	$8.23 \times 10^{18}$	-0.46	$19.0 \times 10^5$
0.5 atom % Fe	$8.34 \times 10^{18}$	-0.51	$17.2 \times 10^5$
1.0 atom % Fe	$3.59 \times 10^{19}$	-0.55	$16.9 \times 10^5$
2.0 atom % Fe	$1.24 \times 10^{21}$	-0.88	$13.9 \times 10^4$
3.0 atom % Fe	$4.53 \times 10^{20}$	-0.68	$16.5 \times 10^4$
4.0 atom % Fe	$1.09 \times 10^{19}$	-0.63	$18.5 \times 10^5$

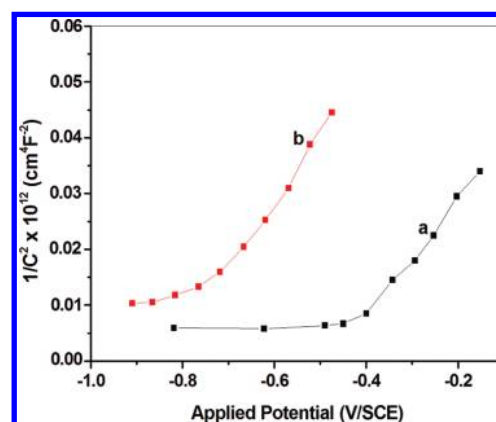


**Figure 11.** Mott–Schottky plots for (a) undoped and (b) 2.0 atom % Fe-doped BaTiO<sub>3</sub>.

density obtained (Table 4; Figure 11). All of the above factors address the better performance of Fe-doped BaTiO<sub>3</sub> in the PEC cell.

## 4. CONCLUSION

Doping of BaTiO<sub>3</sub> with 2.0 atom % Fe is shown experimentally to result in a remarkable increase in the photocurrent density (2.55 mA cm<sup>-2</sup>). The observed change in the electronic band gap and that estimated with first-principles calculations compare well, thus (a) helping understand the origin of the change in the band gap in the impurity band in the gap and (b) suggesting that such calculations have the potential to be used in screening various dopants. This should effectively reduce the number of possibilities promising to yield favorable properties to be tested experimentally. This approach would not only speed up the research efforts but also save lots of chemicals and expenses thereof.

## AUTHOR INFORMATION

### Corresponding Author

\*Phone: +91-9219695960. Fax: +91-562-2801226. E-mail: drsahabdas@gmail.com.

## ACKNOWLEDGMENT

A research grant received from DST-NSTI New Delhi (No. SR/SS/NM-12/2006) is gratefully acknowledged. Support from DST and the U.S. National Science Foundation Material World



Network Program (DST/INT/NSF/MWN/RPO-03/07, NSF DMR-086610) is also acknowledged. We are also thankful to Dr. (Mrs.) Mrinal R. Pai, Mr. Shovit Bhattacharya, and Mr. Sher Singh of BARC (India) for SEM and Mössbauer analysis and Mrs. Meenal, NEERI, Nagpur, India, for DR-UV analysis.

## REFERENCES

- (1) Fujishima, A.; Honda, K. *Nature* **1972**, *238*, 37–38.
- (2) Ashokkumar, M. *Int. J. Hydrogen Energy* **1998**, *23*, 427–438.
- (3) Anpo, M. *Bull. Chem. Soc. Jpn.* **2004**, *77*, 1427–1442.
- (4) Kudo, A. *Int. J. Hydrogen Energy* **2007**, *32*, 2673–2678.
- (5) Maeda, K.; Domen, K. *J. Phys. Chem. C* **2007**, *111*, 7851–7861.
- (6) Osterloh, F. E. *Chem. Mater.* **2008**, *20*, 35–54.
- (7) Sato, S.; White, J. M. *Chem. Phys. Lett.* **1980**, *72*, 83–86.
- (8) Domen, K.; Kudo, A.; Shinozaki, A.; Tanaka, A.; Mariya, K.; Onishi, T. *J. Chem. Soc., Chem. Commun.* **1986**, *4*, 356–357.
- (9) Kudo, A.; Kato, H. *Chem. Lett.* **1997**, *9*, 867–868.
- (10) Sato, J.; Saito, N.; Nishiyama, H.; Inoue, Y. *J. Phys. Chem. B* **2001**, *105*, 6061–6063.
- (11) Elvington, M.; Brown, J.; Arachchige, S. M.; Brewer, K. J. *J. Am. Chem. Soc.* **2007**, *129*, 10644–10645.
- (12) Ikeda, S.; Itani, T.; Nango, K.; Matsumara, M. *Catal. Lett.* **2004**, *98*, 229–233.
- (13) Bae, E.; Choi, W. *J. Phys. Chem. B* **2006**, *110*, 14792–14799.
- (14) Maeda, K.; Teramura, T.; Lu, D. L.; Saito, N.; Inoue, Y.; Domen, K. *Angew. Chem., Int. Ed.* **2006**, *45*, 7806–7809.
- (15) Perharz, G. G.; Dimroth, F.; Wittstadt, U. *Int. J. Hydrogen Energy* **2007**, *32*, 3248–3252.
- (16) Selli, E.; Chiarello, G. L.; Quartarone, E.; Mustarelli, P.; Rossetti, I.; Fornì, L. *Chem. Commun.* **2007**, *47*, 5022–5024.
- (17) Hoffert, M. I.; Caldeira, K.; Benford, G.; Criswell, D. R.; Green, C.; Herzog, H.; Jain, A. K.; Khesghi, H. S.; Lackner, K. S.; Lewis, J. S.; et al. *Science* **2002**, *298*, 981–987.
- (18) Defa, Wang; Jinhua, Ye; Tetsuya, Kako; Takashi, Kimura *J. Phys. Chem. B* **2006**, *32*, 15824–15830.
- (19) Beata, Z.; Ewa, B.-P.; Ryszard, J. K. *Int. J. Hydrogen Energy* **2008**, *33*, 1797–1802.
- (20) Dholam, R.; Patel, N.; Adami, M.; Miotello, A. *Int. J. Hydrogen Energy* **2009**, *39*, 5337–5346.
- (21) Maruska, H. P.; Ghosh, A. K. *Solar Energy Mater.* **1979**, *1*, 237–247.
- (22) Zhang, C.; Wang, C.-L.; Li, J.-C.; Yang, K. *Chin. Phys.* **2007**, *16*, 1422–1428.
- (23) Buscaglia, M. T.; Buscaglia, V.; Viviani, M.; Nanni, P.; Hanuskova, M. *J. Eur. Ceram. Soc.* **2000**, *20*, 1997–2007.
- (24) Stilwell, D. E.; Park, S. M. *J. Electrochem. Soc.* **1982**, *129*, 1501–1506.
- (25) Water Photolysis by Titanates with Tunnel Structures. In *Photocatalysis: Science and Technology*; Inoue, Y.; Kaneko, M.; Okura, I., Eds.; Springer: New York, **2002**; pp 249–260.
- (26) Orhan, E.; Varela, J. A.; Zenatti, A.; Gurgel, M. F. C.; Pontes, F. M.; Leite, E. R.; Longo, E.; Pizanni, P. S.; Beltran, A.; Andres, J. *Phys. Rev. B* **2005**, *71*, 085113.
- (27) Sambrano, J. R.; Orhan, E.; Gurgel, M. F. C.; Campos, A. B.; Goes, M. S.; Paiva-Santos, C. O.; Varela, J. A.; Longo, E. *Chem. Phys. Lett.* **2005**, *402*, 491–496.
- (28) Gurgel, M. F. C.; Espinosa, J. W. M.; Campos, A. B.; Rosa, I. L. V.; Joya, M. R.; Souza, A. G.; Zaghet, M. A.; Pizani, P. S.; Leite, E. R.; Varela, J. A.; et al. *J. Lumin.* **2007**, *126*, 771–778.
- (29) Vinothini, V.; Pramanand, S.; Balasubramaniam, M. *Ceram. Int.* **2006**, *32*, 99–103.
- (30) Moreira, M. L.; Gurgel, M. F. C.; Mambrini, G. P.; Leite, E. R.; Pizani, P. S.; Varela, J. A.; Longo, E. *J. Phys. Chem. A* **2008**, *112*, 8938–8942.
- (31) Baroni, S.; Corsa, D. A.; Gironcoli, S.; Giannozzi, P.; Cavazzoni, C.; Ballabio, G.; Scandolo, S.; Chiarotti, G.; Focher, P.; Pasquarello, A. et al. <http://www.pwscf.org/>
- (32) Vanderbilt, D. *Phys. Rev. B* **1990**, *41*, 7892–7895.
- (33) Hellwege, K. H.; Hellwege, A. M. *Ferroelectrics and Related Substances*; Springer: Berlin, 1960; New Series Group III vol. 3.
- (34) Monkhorst, H. J.; Pack, J. D. *Phys. Rev. B* **1976**, *13*, 5188–5192.
- (35) Inas, K.; Battisha, A. B.; Abou, H.; Ragab, M.; Mahani, R. M. *Physica B* **2009**, *404*, 2274–2279.
- (36) Buscaglia, M. T.; Buscaglia, Y.; Viviani, M.; Nanni, P.; Hanuskova, M. *J. Eur. Ceram. Soc.* **2007**, *20*, 1997–2007.
- (37) Taguchi, H.; Masunaga, Y.; Hirota, K.; Yamaguchi, O. *Mater. Res. Bull.* **2005**, *40*, 773–780.
- (38) Gupta, M.; Sharma, V.; Shrivastava, J.; Solanki, A.; Singh, A. P.; Satsangi, V. R.; Dass, S.; Shrivastava, R. *Bull. Mater. Sci.* **2009**, *32*, 1–8.
- (39) Pontes, F. M.; Pinheiro, C. D.; Longo, E.; Leite, E. R.; de Lazaro, S. R.; Magnani, R.; Pizani, P. S.; Boschi, T. M.; Lanciotti, F. *J. Lumin.* **2003**, *104*, 175–185.
- (40) Greenwood, N. N.; Gibbs, T. C. *Mössbauer Spectroscopy*; Chapman and Hall Ltd.: London, 1971; pp 465–468.
- (41) Fangting, L.; Dongmei, J.; Xueming, M.; Wangzhou, S. *J. Magn. Mater.* **2008**, *320*, 691–694.
- (42) Bhide, V. G.; Multani, M. S. *Phys. Rev.* **1966**, *149*, 289–295.
- (43) Mashkina, E.; McCammon, C.; Seifert, F. *J. Solid State Chem.* **2004**, *177*, 262–267.
- (44) McCammon, C. A. In *Transformation Processes in Minerals*; Redfern, S., Carpenter, M., Eds.; Mineralogical Society of America: Washington, DC, 2000; pp 241–264.
- (45) Chang, H.; Kong, K.; Choi, Y. S.; In, E.; Choi, Y.; Baeg, J. O.; Moon, S. J. *Chem. Phys. Lett.* **2004**, *398*, 449–452.
- (46) Singh, A. P.; Kumari, S.; Shrivastav, R.; Dass, S.; Satsangi, V. R. *Int. J. Hydrogen Energy* **2008**, *33*, 5363–5368.
- (47) Kumari, S.; Chaudhary, Y. S.; Agnihotry, S. A.; Tripathi, C.; Verma, A.; Chauhan, D.; Shrivastav, R.; Dass, S.; Satsangi, V. R. *Int. J. Hydrogen Energy* **2007**, *32*, 1299–1302.
- (48) Chien-Cheng, T.; Hsisheng, T. *Appl. Surf. Sci.* **2008**, *254*, 4912–4918.
- (49) Marinova, V.; Lin, V.; Sainov, V.; Gospodinov, M.; Hsu, K. Y. *J. Opt. A: Pure Appl. Opt.* **2003**, *5*, 500–506.
- (50) Hu, Y. S.; Shwarsstein, A. K.; Forman, A. J.; Hazen, D.; Park, J. N.; McFarland, E. W. *Chem. Mater.* **2008**, *20*, 3803–3805.